Observations of nonlinear run-up patterns on plane and rhythmic beach morphology

K.R. Bryan[1*] and Giovanni Coco[2]

1 University of Waikato, Hamilton, New Zealand

* corresponding author

2 National Institute of Water and Atmosphere Research, Hamilton, New Zealand

Abstract:

Application of non-linear forecasting and bispectral analysis to video observations of run-up over cuspate topography shows that these alongshore patterns in the morphology are accompanied by changes to the fundamental behaviour of the run-up timeseries. Nonlinear forecasting indicates that at beach cusp horns, the behaviour of swash flow is more predictable and global (meaning that characteristics of individual swash events are well represented by the behaviour of the timeseries as a whole). Conversely, at beach cusp bays, the behaviour of swash flow is less predictable and more local (meaning that the characteristics of individual swash events are best represented by the behaviour of a small fraction of the timeseries). Bispectral analysis indicates that there is a nonlinear transfer of energy from the incident wave frequency f to infragravity frequency $\sim f/2$ which only occurs in the bay, suggesting that the local behaviour is caused by interactions between successive swash cycles which are magnified by channelling caused by the beach cusp geometry. The local behaviour and the bispectral signatures are not present in offshore measurements, and are not present in runup timeseries collected when the beach was planar. These results provide evidence that interactions between successive run-ups are a fundamental characteristic of beach cusp bays. Ultimately, these interactions could lead to the growth of an infragravity wave with an alongshore wavelength forced by the presence of beach cusps.

Introduction

The swash zone is the area where the movement of the waterline runs up (covers) and down (uncovers) the beachface with the passing of incoming waves. Swash movements form a critical part of the link between the ocean and the beach face which ultimately determine the nature and severity of the erosion hazard during storm events. The key controls on the swash amplitude are the energy input at incident wave frequencies into the surfzone but also the processes inside the surfzone removing and transferring energy between frequencies, and finally the interaction between waves and beachface morphology at the shoreline. Field measurements of run-up (the swash edge) spectra show that saturation occurs in the incident wave frequency range with increasing incident wave height, so that during storm events, this component of run-up has no preferred incident peak and is limited in size [*Raubenheimer and Guza,* 1996]. Observations (both field and laboratory) of swash amplitude over a wide range of saturated (non-reflective) conditions show a sensitivity to the square of beach slope β [*Huntley et al.*, 1977; *Mase*, 1988; *Raubenheimer and Guza,* 1996]. Conversely, infragravity levels in swash time series can be large, particularly during storms, sometimes exceeding incident wave energy levels [*Raubenheimer and Guza*, 1996].

In general, field studies of infragravity signals in run-up have been undertaken on beaches with little alongshore rhythmicity (e.g. *Ruggiero et al.* [2004]). However cuspate topography quite commonly develops on intermediate beaches after storm events [*Coco et al.,* 1999]. Conceptual models show that alongshore variations to beachface morphology can force alongshore variations in swash flow behaviour, sometimes causing the up-rush to split at the cusp horns (that protrude seaward, with higher beach slopes) and collect in concentrated down-rush channels in the bays (which have relatively lower beach slopes) [*Masselink and Pattiaratchi,* 1998]. The overall effect of the morphology is an alongshore hydrodynamic patterning in the swash at incident wave scales

which has an alongshore modulation driven by the beach cusp morphology [*Holland and Holman*, 1996; *Masselink and Pattiaratchi*, 1998].

Video observations [*Ciriano et al.*, 2005] and resistance run-up wires [*Masselink et al*., 1997] have been used to show that, when beach cusps are present, horn-bay differences occur in both the incident and infragravity range of the swash spectrum with more (less) energy at horns (bays) at incident wave frequencies and the reverse occurring at infragravity frequencies. The incident wave pattern is easily related to the steeper-sloped cusp horns causing reduced swash excursions relative to at the bays, a pattern simply driven by the control on run-up amplitudes by slope β. However, the source of the infragravity patterning is more intriguing. The infragravity energy observed in *Ciriano et al.* [2005] was also shown to propagate alongshore with edge-wave-like speeds and to increase with growth in cusp height. Indeed, beach cusps can theoretically provide the scale needed to force alongshore patterning in the infragravity waves (e.g. edge-waves) [*Bowen*, 1997]. *Holland and Holman* [1996] also show evidence of infragravity energy with the same alongshore scale as an existing field of beach cusps, which may have been excited by the interaction between morphology and swash motions.

In both *Ciriano et al.* [2005] and *Holland and Holman* [1996], the source of the infragravity patterning was not successfully resolved. The short alongshore range of the measurements (3–4 beach cusps in *Ciriano et al.* [2005] and 4–5 in *Holland and Holman* [1996]), the elevated noise levels associated with the waterline detection from video and the complexity of the patterns caused by the channelling and swash interactions make it difficult to detect and understand patterns with the linear timeseries techniques employed in those studies. Also, the maximum likelihood technique used in *Ciriano et al.* [2005] was developed for linear waves measured using an alongshore array of current meters or pressure sensors. Conversely, swash cycles are often roughly parabolic (rather than sinusoidal) and the cross-shore location of the measurements

collected using the video over cuspate topography varies, more seaward over horns and landward over bays. Clearly there is scope for examining these observations using different techniques.

There are a number of analysis methods available for understanding processes in time series which do not assume linearity or even weak non-linearity, which may be more appropriate for application to swash time series. Bispectral analysis has been used extensively in the surf zone to study the non-linear transfer of energy between frequencies [*Hasselmann et al*., 1963; *Elgar and Guza*, 1985; *Herbers et al*., 2000]. This transfer is measured by the coherence and phase of phase coupling between frequencies. For example, the bi-spectral signature $B(f_1,f_2)$ of a Stokes wave is a coherent signal at $(f,f$ (which indicates energy transfer between f and $2f$)), $(f,2f)$, $(2f,2f)$, and so on, with a phase of zero [*Elgar and Guza*, 1985], where $f=1/T$ and T is the wave period. The detractions of bispectral techniques are the assumption of stationarity, and the larger data requirements for statistical stability compared to spectral analysis [*Elgar and Guza*, 1985]. The resulting properties (e.g. the existence of coherent energy peaks, the period at which these peaks occur) are representative of the global properties of the timeseries. However, the interaction between flow and morphology resulting in channelised down-rushes and the splitting up-rushes may not necessarily be a stationary process. Such local variations in the timeseries would simply widen the bispectral signatures.

A technique that has been developed to assess the relative contribution of the global versus the local properties in a timeseries is non-linear forecasting [*Farmer and Sidorowich*, 1987; *Sugihara and May*, 1990]. This has been used to examine the behaviour of a wide range of natural time series, for which techniques that require stationarity have provided limited insight, for example, phytoplankton population dynamics [*Sugihara*, 1994], the electrical precursor signals to earthquakes [*Cuomo et al*. 1998], synthetic swash-time series [*Bryan and Coco*, 2007], surf-zone bar behaviour [*Holland et al.,* 1999; *Pape and Ruessink*, 2008] and surf zone suspended sediment

patterns [*Jaffe and Rubin*, 1996]. The technique is based on the premise that, if the statistical properties of the time series vary locally, a simple data-driven model will perform better if only trained using a fraction of the available training dataset. If, in the case of swash, the properties of the timeseries change after the occurrence of a swash interaction, then a model will provide better predictions for the post-interaction behaviour if trained only on sequences of waves that were similar to the sequence of events that lead to the swash interactions. If swash interactions do not cause local variations in the timeseries, then there would be no difference between the model trained this way, and the model trained using all the available training dataset.

In this paper, we will identify and examine spatial patterns in swash hydrodynamic behaviour associated with beach cusps using bispectral and non-linear forecasting techniques and will provide insight into the underlying physical processes related to these spatial patterns.

Methods

Data collection

The data were collected during the Duck94 field experiment at Duck, North Carolina and have been presented previously [*Elgar et al*., 1997; *Coco et al*., 2003; *Ciriano et al*., 2005]. Offshore sea-surface elevation timeseries were collected during the experiment at 2Hz using a cross-shore array of 15 pressure sensors which extended some 750 m seaward, spanning the single bar which was located approximately 100 m offshore. Run-up measurements were extracted at 2Hz from video imagery at 19 alongshore positions which were separated by 10m intervals. Run-up observations were available only during daytime and were split into 2 hour bursts (each burst containing approximately 14,000 points). The cross-shore array intersected the alongshore array at the edge of alongshore field of view of the video system used to collect swash measurements. The beachface was surveyed using standard staff and level techniques, and the surveys were used to translate the swash measurements into elevations. The offshore bathymetry was surveyed daily using a 10-m high amphibious buggy to carry the survey prism offshore (see *Gallagher et al*. [1996] for a description). Cross-shore array timeseries were divided into bursts coinciding with the 14,000 point run-up timeseries. Video and sea surface elevation data were not synchronised. Sea surface and run-up timeseries were reduced to the same datum.

Four datasets were selected for detailed analysis. Two were taken at high and low tide on a day (September 6th, 1994) in which the beach had strongly-cusped topography (with stronger flow-morphology interaction at high tide than at low tide), and two were taken at high and low tide on a day in which the beach had no cusps (September 4th, 1994). Although ideally a controlled experiment would have the same offshore forcing conditions, this was not the case as the significant wave height and periods from the directional wave array in 8-m of water depth (http://www.frf.usace.army.mil/) were 2.8m and 9.7s and. 0.9m and 12.0s for September 4th and 6th respectively.

Data analysis

The aim of this work was to investigate the cause of alongshore variation in run-up timeseries using nonlinear timeseries techniques. Thus, run-up and offshore timeseries were analysed by (1) calculating bispectra (following *Elgar and Guza* [1985] and (2) by using non-linear forecasting (following *Sugihara and May* [1990]).

The terminology ‘non-linearity’ is used differently in different fields, and deserves a definition for the context of this work. In studies of waves, a non-linear wave is one in which significant energy has transferred to phase-locked higher-order harmonics so that the shape of the wave is skewed or asymmetric, accompanied by a skewed probability density function. Throughout this work the use of the term “non-linear” is broader as, in an idealised situation, it is possible to have timeseries of skewed/asymmetric waves in which each cycle is identical, e.g. its global properties are the same as its local properties (apart from at sub-wave scales where each trough is locally different than each crest). On the other hand, the growth of an instability, such as can occur in deep water waves, can result in the non-linearity being manifest as local behaviour in the timeseries (e.g. an unusually large wave). This type of nonlinearity in timeseries can be studied using a measure of the degree of localness. Non-linear forecasting is a technique that is commonly used to detect degrees of localness. This localness in the timeseries is different than the variations between wave cycles in the timeseries that are caused by the random nature of waves (for example, group structure in waves) as the latter does not cause repeatable sequencing of waves in the timeseries, whereas the former does.

In nonlinear forecasting, a simple statistical model is used which is fit to portions of the timeseries of varying size. If the model performs better when fit only to a small portion of the available timeseries, then the timeseries has local characteristics and if the model performs better

when fit using the whole timeseries, then it has global characteristics. In most cases the model used is a linear auto-regressive model [e.g. *Rubin* 1992; *Rubin*, 1995; *Bryan and Coco*, 2007], but can be nonlinear (see review in *Abarbanel* [1986]) or depend on second independent timeseries such as a forcing timeseries [*Jaffe and Rubin*, 1996; *Pape and Ruessink*, 2008]. Here, we use the simplest form, an autoregressive model, to forecast the timeseries, x at time t, into future timesteps d

$$x(t + d\Delta t) = a_o + \sum_{j=0}^{j=m-1} a_{j+1} x(t - j\Delta t) \qquad (1)$$

where Δt is the time lag between points, a_{j+1} are coefficients and m is the length of the sequences used to make the forecast (plaquette size or embedding dimension). The goal here is a relative comparison of model fits rather than to optimise prediction ability, so the simple model is sufficient. The model is fit using sequences of points which display similar local behaviour (nearest neighbours k), where nearest neighbourhoods are evaluated by calculating the Euclidian norm. The number of nearest neighbours is varied systematically and the performance of the model is evaluated using either the forecasting error or the correlation between forecast and observations. In natural timeseries, the performance of the forecast diminishes as the forecast is driven into the future. The optimum m, k and performance of the forecast with distance d into the future can be used as a diagnostic statistic, ideally giving indications of the underlying nature of the processes. Optimum fits found at smaller k indicate that local behaviour dominates the timeseries (and conversely optimum fits at maximum k indicate that global behaviour dominates the timeseries). Synthetic tests using inherently local timeseries, indicate that if the data are noisy, the global model fit can still be optimum as it best suppresses noise [*Rubin*, 1995].

The time lag Δt is calculated using the first minimum in the average mutual information [e.g. *Abarbanel*, 1986]. The average mutual information is a quantity used to establish the connection

between two sets of measurements and determines the temporal lag that maximizes independence of measurements while still retaining useful information about nonlinearity. Its counterpart in the linear field is linear autocorrelation, although it has been shown [*Abarbanel*, 1986] that using the first minimum in linear autocorrelation can be misleading and hinder the examination of nonlinearities in the timeseries. Note that the time lag Δt used in the analysis is not the same as the sampling interval with which the data were collected (which is 0.5 s).

The forecasting was implemented using five thousand sequences of points that were randomly selected (insuring no repeat selections) from the timeseries to test the performance of the forecast. In each case, the model was trained using the remaining sequences of points as nearest neighbours (e.g. with all the points between $t-(m-1)\,\Delta t$ and $t+d\Delta t$ removed). Nearest neighbours were recalculated for each prediction d. The average correlation between forecast and observations was evaluated using these 5000 test cases. This process was repeated while searching for the optimum combination of m and k.

The 95% significance level for the correlation between prediction and observation was assessed by randomising the timeseries prior running the forecasting technique using 500 test cases (rather than the customary 5000 test cases). This process was repeated 100 times at every k, d, and m to find the 95% significance levels for each k, d and m. The process of calculating significance levels was time-consuming and was undertaken only on two timeseries, one from the horn and one from the bay. The use of randomized timeseries showed no preferred k and m in the correlation between predictions and observations.

Tests with synthetic timeseries

Although nonlinear forecasting has been used for a wide range of timeseries, including many examples of natural timeseries, the extension to naturally cyclic series is not straightforward since

it is necessary to control for the confounding effect of the autoregressive behaviour which results from the shape of the cycle [*Bryan and Coco*, 2007]. A forecast in which the prediction distance *d* is less than *T*, where *T* is the wave period, will be better forecast with a smaller *k*, because there is enough information in the plaquette or sequence $x(t-j\Delta t)$ on the evolution of that cycle to train the model by finding similar cycles from the training dataset (if the plaquette contains a small trough, the training dataset will indicate that a small crest is likely to follow). In this case, local behaviour in the series (although still useful information) cannot be attributed to a nonlinear process, but simply to the degree of random variability in wave cycles in the timeseries [*Bryan and Coco*, 2007]. Conversely, in the case of a forecast in which $d>T$, the plaquette contains no information from the cycle to be predicted, and so the local model will only be better than the global model if there are local sequences of wave cycles that are repeated in the training dataset (for example, a sequence of 2 small crests then a large crest). If the waves sequence is completely random, then the global model will prevail, as it will predict a wave cycle using the average characteristics of the timeseries. The interest in this work is in the sequencing of swash cycles (not the variability within swash cycles), so the $d>T$ forecasts are the relevant ones.

To demonstrate these points and to compare forecasting to spectral and bispectral analysis, 10 synthetic timeseries were generated, characterized by the same number of points and sampling frequency as the observed timeseries. The first 5 timeseries were: (1) a timeseries with a narrow-banded spectrum, reconstructed using randomised phases (Figure 1.A1) (2) a timeseries with a broad-banded spectrum, reconstructed using randomised phases (this case is similar to the measured run-up spectra) (Figure 1.A2) (3) a Stokes wave in which each cycle was an exact copy (Figure1.A3) (4) an inverted Stokes wave in which every second cycle was larger (the Stokes waves were inverted to roughly imitate the shape of a swash cycle) (Figure 1.A4) (5) a random mixture of sequences of inverted Stokes waves all with the same height and period and case (4) (Figure 1.A5). The last case was included to artificially induce localness in the timeseries. *Bryan*

and Coco [2007] show other types of synthetic tests designed to test whether the results were significant relative to a timeseries with cycles of similar parabolic shape, but with random ordering of swash cycles (following recommendations for autocorrelated timeseries, e.g. *Small and Tse* [2002]).

The remaining 5 synthetic timeseries were generated to simulate swash timeseries. In this case, each swash cycle was evolved using the Shen and Meyer solution for a single swash front moving up and down a plane beach [*Shen and Meyer*, 1963]. Beach slope (=0.01) and incoming wave period (=7s) were chosen to insure the downrush was not completed prior to the initiation of the next uprush. The starting velocity and the starting location of each swash front and the period of the forcing were randomly varied. To simulate swash interactions, the starting velocity was made to be dependant on the down-rush velocity of the previous swash cycle, to varying degrees. The cases that were constructed were: Case 6 (Figure 2.A1) in which the starting velocity, starting location and forcing period were varied randomly, but with no interaction between swashes; Case 7 (Figure 2.A2) where conditions were not varied, but an infragravity wave superimposed; Case 8 (Figure 2.A3) where the degree of the random variations in conditions were modulated with time, and there was a weak interaction between swash cycles; Case 9 (Figure 2.A4) which was the same as Case 8, only the interaction was strengthened; Case 10, which was the same as Case 9, only the degree to which the randomness in conditions varied was increased. These cases were chosen as a best simple guess of the type of time series which might occur naturally. The shortcomings of the Shen and Meyer swash model, and inadequacy of the synthetic interaction term are recognised.

In Cases 1 and 2, where timeseries were reconstructed from spectra using randomised phases, bispectral analysis indicated these series were linear (with no coherent signal at any of the frequency combinations, Figures 1.B1 and 1.B2). In the case of the narrow-banded forecast, the

local and global model gave essentially the same forecast, and the timeseries were well predicted. (Compare the correlation obtained using small numbers of nearest neighbours k in Figure1.D1 to that obtained using large k). This is because each cycle is so similar, that there is no advantage to being able to train the model to the local characteristics of the timeseries. In the case of broad-banded random-phased series, the cycles vary much more, and so predictive power is much reduced (note the lower correlations in Figure1.D2). However, because the variation of each cycle is randomly distributed around the mean cycle (and there is no particular local pattern of sequences of cycles) the optimum model is again based on the global characteristics of the average cycle. The bispectral signature of the Stokes wave (Case 3) is phase-locking between the fundamental and harmonic, represented as high coherence levels at (f,f) and (f,2f) and so on (Figure 1.A3). The forecasting signature of a Stokes wave (or an asymmetric wave) associates slightly higher correlations to local models, which disappears if plaquettes that are much longer than a wave cycle are used (Figure 1.D4). The case of alternate sized wave heights is represented in the bispectra analysis as a coherent peak at exactly (f/2,f/2) (Figure 1.B4). Alternating this timeseries randomly with portions of constant height series, smears this sharp peak into a line along which $f_1+f_2=f$ and also $f_1+f_2=f/2$ (where f_1 and f_2 are the frequencies of the waves which are receiving energy from the incident waves) (Figure1.D5). The forecasting signature of Case 4 is a slight enhancement of the local model over the global, whereas the forecasting signature of Case 5 contains stronger evidence of local behaviour. In fact, the synthetic series created in Case 5 is not strongly local as the period and shape of each wave cycle are the same, and are global characteristics, only the height is locally varying, and only varying between 3 heights (Figure 1.A5). Figure 1.C shows the spectrum for each case for reference. The dependence of the performance of the local versus the global model as a function of the percentage of mixture used to create Case 5 is shown in Figure 3. Other works have also shown the power of non-linear forecasting to detect locality of timeseries [*Rubin*, 1992; 1995].

All the synthetic cases in the second group of Cases (Figure 2) have some infragravity energy in the spectra (Figure 2C). However, forecasting, and to a lesser extent, the bispectral results are quite different in each case. The random modulation of the starting conditions of each modelled swash cycle means that some swash cycles do not complete before the subsequent swash cycles start. This causes an infragravity signal that is generated is phase locked to the incident swash cycles (the evidence is the coherence at (*f/2*,*f/2*) in Figure 2.B1). Conversely, the case with a superimposed infragravity signal is not phase locked (Figure 2. B2). In Cases 8–10, there is evidence of the phase-locking, but it is not possible to separate the role of the interaction (as in Cases 4 and 5) from the role of the modulating starting conditions. The forecasting, however, can differentiate between these processes, Case 6 is clearly global (Figure 2.D1) where as Cases 8–10 are local. In fact, the stronger interaction in Case 9 relative to Case 8 is manifest as a lower optimal *k* (and to a lesser extend optimal *m*). The levels of correlation in the timeseries are completely controllable by the degree of randomness added to the model (compare Cases 9 and 10, Figure 2.D4 and Figure 2.D5). The degree of localness can also be measured by the correlation ρ difference between the optimal model $\rho(k_{opt})$ and the global model $\rho(k_{gobal})$, however this is quite difficult to control in the synthetic cases. Superimposing global randomness reduces the correlation (Cases 2 and 6), increasing local randomness both increases the enhancement, and reduces the correlation (Case 10). The synthetic results are summarised in Table 1.

In summary, spectral and bispectral analysis provide an average statistic of the whole series (a ‘global’ statistic). Sequencing of swash cycles in the timeseries causes a coherent coupling at infragravity frequencies in the bispectrum, regardless of whether the sequences are a global or local characteristic. Local variations in height and period over the duration of the timeseries appear to cause a broadening or blurring of the main spectral/bispectral peaks. Only the

forecasting analysis can differentiate consistently between sequencing that is local and sequencing that is global.

Results

The surfzone pressure gauge timeseries collected when beach cusps were present (September 6th) show that the wave period decreased inside the surf-zone as the waves became asymmetric (see *Elgar et al*. [1997] and Figure 4, middle and bottom panels). As the waves change shape, they transfer energy to their harmonics, which eventually become separate crests from the fundamental shape. The period then lengthens again in the run-up timeseries. The spectra (Figure 5, middle and bottom panels) also show an increase in harmonic energy in the surf zone spectra. The run-up timeseries shown in Figure 4 (left panel), are synchronised and so show the difference in run-up as the wave interacts with a horn and with a bay. It also shows that there are sequences of small followed by large run-up cycles (Figure 4, Left middle panel, at 60-70 seconds). The run-up spectra from September 6th have a distinct peak at incident wave frequencies, decaying with increasing frequency to a rate proportional to between f^{-3} and f^{-4} until eventually flattening to a noise floor at $f > 0.5$Hz (not shown). Although there are some differences between horn and bay spectra, where bays have more energy at infragravity (and less energy at incident) wave frequencies than horns (also shown in *Masselink et al*. [1997] and *Ciriano et al*. [2005]), the differences between the infragravity horn and bay spectra in Figure 5 are not significant. The differences between bays and horns are less apparent at low tide, when the interaction between morphology and flow over beach cusps is less prominent. Conversely, on the day when there were no beach cusps (Figure 4, top panel), there is much less alongshore variability in the run-up timeseries and spectra. The incident wave peak disappeared in the inshore spectra on September 4th, because of increased breaking on the inside of the bar on this higher wave energy day. The run-up spectra are saturated with little evidence of an incident wave peak. Infragravity energy increased shoreward on both days, and was greater on the day with larger incident wave energy (Figure 5, right panels).

Nonlinear Forecasting results-Run-up timeseries

The non-linear forecasting results for the run-up timeseries over beach cusps (September 6th) showed distinct alongshore patterns which matched the spacing of the cusps both in the level of correlation attained (and the rate at which this correlation decayed with d), but also in the optimum embedding dimension m and numbers of nearest neighbours k. Figure 6 shows examples of the two extremes. The left panel shows the case obtained using a typical timeseries from the horn in which the correlation at optimum k and m is ~0.65. Conversely the right panel shows a typical result using a timeseries from the bay, where much lower correlations corresponded to lower values of optimum k and m. There is also a greater difference between the correlations obtained with the global (maximum k) and local models (optimum k) in the case collected at the bay (see enhancement factor summarised in Table 1). To reduce variability in the results, a 4th order polynomial surface was fit to the results and used to find the optimum k and m (see marked circles on Figure 6). Note that the maxima are broad (although k is plotted on a log scale), so the precise value of the optimum k is less relevant than the pattern of variation. The 5% and 95% significance levels are not plotted on any of the results figures, but amount to approximately ±0.05 (so that correlations of greater than 0.05 and less than -0.05 are significantly different from 0). For clarity, we employed different greyscales in each figure.

Figure 7 (centre panel) shows the decay of the correlation (greyscale) with increasing forecasting distance into the future d at the optimal nearest neighbour k and embedding dimension m, along with the value of the optimal k (black line). The lag time Δt varied between 7 points at the horns and 10 points at the bays at high tide, and 6 and 8 respectively at low tide. (The results reported here are not sensitive to the lag time choice, and a $\Delta t=1$ gives a very similar results, however the larger lag times increase computational speed dramatically). Disregarding the results where $d <$ 12s (the run-up period), which are driven by variability of the shape of the swash (see *Bryan and Coco* [2007]), a plaquette size m of 4 is optimal in the bays at high tide, which equates to the plaquette spanning $4\Delta t$=40 points or 20 s, which is larger than a swash cycle (approximately 2

swash cycles). At horns, the plaquette spans ~ 25 s, which is slightly more than 2 swash cycles. At low tide, the plaquette is larger, but combined with the smaller Δt ultimately results in a similar temporal span. The optimum k varies similarly with alongshore location, where 9% of the series were similar enough to provide the best prediction in bays, whereas at horns the similarity increases to 18% of the series (Table 1). The alongshore variations in local/global behaviour are clearly related to the geometry of beach cusps (Figure 7). Conversely, at low tide swash flow operates at lower elevations on the beachface where flow-morphology interactions are less strong, and so is the alongshore patterning in the forecasting results (Figure 7).

In Figure 8, the results obtained using the timeseries at and on either side of the horn and bay are averaged to make a representative result for the horn and for the bay (they are also averaged in Table 1). High tide bay correlations are identical to low tide correlations for either horn or bay (Figure 8A). As the correlations diminish with distance into the future, the optimum k and m values (Figure 7B and C respectively) increase as the more global models are able to cope with noise which becomes more prevalent at large d [*Bryan and Coco*, 2007]. More local models (smaller k and m) produce better predictions at the bays whereas more global models are optimal at the horns. Also, the optimal models for both horns and bays are generally more local at high tide where the cusps induce stronger run-down/run-up interactions than at low tide. To summarise, Figure 9 shows the correlation, optimum m and k values plotted against the steepest local foreshore gradient where that timeseries was collected (at the '+' lines marked on Figure 7A, which represent one standard deviation above the level of mean swash). The dependence on beach cusp slope is evident.

When the same analysis is repeated using the run-up timeseries collected when there were no beach cusps present (September 4th), there are no substantial alongshore patterns in the

forecasting results (Figure 10, note the different scale for *k,* and Table 1). Moreover the correlations are lower than either case from September 6th.

Nonlinear Forecasting results - Offshore timeseries

A question arises: is the local behaviour associated with high tide timeseries on September 6th an indication of processes in the swash zone, or is it simply a reflection of nature of the incoming wave field? The non-linear forecasting analysis was run on 4 offshore sea-surface elevation timeseries at all 15 cross-shore locations, corresponding to a low and a high tide case from September 4th and 6th (Figure 11). For consistency, the analysis was performed in the same way as for the run-up series.

Seaward of the bar, the correlations between the forecast and the timeseries are slightly higher at high tide than low tide (compare solid (high tide) versus dashed lines (low-tide) in Figure 11C), and higher on the lower energy day (compare lines (lower energy) to lines with stars (higher energy)). When the waves break over the bar at low tide and also at high tide on the higher wave energy cases, correlation drops to 0.15-0.25 landward of the bar. The extremely low correlations at the most in-shore sensor at low tide are below the significance level, and are associated with the sensor surfacing during the passing of wave troughs; these correlations should be disregarded. At high tide on the less energetic day, the correlation drops only at the most inshore sensor (which is always underwater). Presumably in this case, the waves do not break over the bar, but break only as they approach the beach face. Note that the cross-shore array intersects the alongshore array half way between a horn and bay (thick solid line on Figure 7A).

The optimum number of nearest neighbours is markedly different for $d<T$ and $d>T$ (Figure 11A and B). For $d>T$, the best model is the global model in all cases, indicating that the sequencing of waves is random, and there is no local structure. This is different from the forecasting results

from analysis of the run-up series (Figure 8B). When $d<T$, the optimum number of nearest neighbours varies depending on tidal stage and wave height, with the most global timeseries being from the offshore timeseries on September 6th, collected at high tide, and the most local being from the inshore series collected at the same time. As stated previously, these patterns relate to the variability in the shape of swash caused by changes to the broad-bandedness.

Bispectral Analysis

The bispectral analysis provided some additional insight into alongshore patterning in the run-up series. As with the forecasting results, there were distinct differences between the horns and bays. Both horn and bay results had coherent peaks at (f,f), (f,2f), consistent with the characteristic shape of run-up cycles (Figure 12 C–F). The phase relationship at these peaks was 50 degrees, which was not similar to the results obtained using the inverted Stokes waves (Figure 1.D3), so clearly the up-rush and down-rush are not symmetric. More work is needed to determine whether the asymmetry and the differences that exist between horns and bays are genuine or relate to differences in the video-detection of run-up and run-down.

The interesting pattern lies in the coupling between infragravity and incident waves (f/2,f/2). This shows a peak in the bispectral coherence which is similar to the peak observed in synthetic Case 4 (Figure 1), only broadened along a line like the lower frequency signatures shown with Cases 5, 7, 8 and 9. This peak is only evident in the run-up collected over bays (Figure 12B, solid line). Moreover, there is a consistent pattern in the phase that also relates to the beach geometry (Figure 12B, dashed line). These bispectral signatures are not present in any of the offshore timeseries, or in the run-up timeseries collected on September 4th (not shown), suggesting that the coupling is not due to the influence of variability in the incoming wave conditions (e.g. like in Case 6, Figure 2) that might by caused by group structure.

Discussion

There is evidence that the run-up is shaped by the cuspate topography and this affect causes an alongshore variation in the non-linear properties, both in terms of the bispectral signatures and the existence of local behaviour in the timeseries.

The forecasting results show that swash timeseries collected near beach cusp bays are better predicted by a more local model (Figure 7), in contrast to horn timeseries which behave more globally. The forecasting results at $d<$ average swash period are an indication of the model's ability to predict the evolution of a single swash cycle given some information from that same swash cycle. The forecasting results $d>$average period are an indication of the model's ability to predict the next swash cycle given information of previous swash cycles. The superior performance of the local model means that there are repeatable local patterns in the shape or sequence of swash cycles that differ from those in the time series as a whole. The globality of the model gradually increases (*m* and *k* increase) in all cases (both swash and offshore timeseries) with prediction distance into the future. This is generally true of all series with a random component and not an indication that the nature of the underlying process necessarily changes to become more global, but just that the noise component becomes increasingly dominant [*Rubin*, 1995]. Uncorrelated noise makes a time series more global for all prediction distances into the future. Uncorrelated noise (such as addition of random numbers) will not cause predictions to degrade into the future, but brown noise (addition of a running sum of random numbers) will.

One explanation for the local behaviour exhibited in run-up timeseries is that it is related to interactions between run-up cycles. As the swash runs up the beach face, its motion is retarded by gravity and friction. It eventually slows to a halt, and begins to move down the beach face as a down-rush. Depending on the time taken for this movement up and down the beach face, the down rush can interact with the up-rush of the next wave. This interaction means that the

amplitude of the new uprush will depend not only on the amplitude and period of the incoming wave, but also on the amplitude and period of the previous wave(s). Thus a forecasting model which is tailored to the evolution of similar sequences of previous swash events (including interactions between them) will inevitably provide a better prediction then one that is driven by the general characteristics of the timeseries. This explanation is consistent with the synthetic tests that are presented in Figure 1 and 2 (Cases 4,5,8,9,10).

It is not possible to attribute all the local behaviour in the forecasting results simply to the lower beachface slope at cusp bays, because there is also a tidal dependence in the optimal type of forecasting model (Figure 8, d>12s). As the tide decreases, the beach that influences the run-up is flatter (Figures 7, Left Panel, and 9), and thus the run-up amplitude should increase relative to the incident wave period and make interactions more likely. However, the optimum m and k increase (Figure 8, d>12s), so the timeseries is better predicted by a more global model, despite the decrease in slope.

A key difference between high and low tide on September 6th, is a decrease in the morphology-flow interaction as the waterline moves down the beach face. Presumably, the convergence of water particles caused by beach cusps causes a channelling of the down-rush in the bays, and this process contributes to swash interactions and local behaviour in the cusp bays at high tide. Convergence increases the force of swash interactions in bays so that the evolution of each run-up cycle is even more dependant on the size of the previous sequence of run-up cycles than without the influence of cusps. Thus swash behaviour is generally more local in the presence of beach cusps then on a beach with a similar slope but no cusps.

It is possible that the high-low ordering that causes the coupling between incident and sub-harmonic frequencies in the bay is caused by the bimodality of the wave spectrum in the surfzone

at high tide (Figures 4 and 5). A succession of alternating high and low waves is evident in the timeseries of both inshore sea surface elevation and the high tide run-up (Figure 4). The offshore bimodality is certainly related to asymmetric shape of the waves in the trough. These waves separate from the fundamental wave shape and become individual waves as they propagate shoreward [*Elgar et al.,* 1997, and also evident in Figure 4]. This bimodality is evident in probably density functions of wave crest height and swash crest height at high tide (not shown). However, there is no evidence of high-low ordering in the bispectra from the offshore timeseries anywhere (Table 1). The synthetic results in Figure 1.B4 indicate that a consistent high-low ordering appears in the bispectra as a phase locking between the incident and sub-harmonic. Therefore the high-low ordering in the swash timeseries cannot be driven by the freely propagating harmonics in the incoming wave field.

The bispectra analysis does show that there is an infragravity pattern in the bay which is a wave at approximate $f/2$ that is phase-locked to the incident waves (Figure 12). The synthetic tests show that this is qualitatively consistent with a pattern of alternating high and low run-ups which are interspersed with periods of no sequencing (Cases 4,5,7,8,9). This, coupled with the forecasting results, suggest that the channelised downrush is interacting to suppress subsequent up-rushes in the cusp bays. These up-rushes are then smaller, and cause smaller down-rushes, thus the sequence of high and low run-ups evolves in the bay. The significance of the phase-locking is that it provides a mechanism for transfer of energy from incident wave frequencies to infragravity frequencies, thereby explaining the increase in infragravity and decrease in incident wave energy observed over cusped topography [*Ciriano et al*., 2005; *Masselink et al*., 1997]. This infragravity wave that is excited by this coupling mechanism will have the alongshore wave length of the cusp topography, and may explain why *Ciriano et al.* [2005] observed increased edge-wave like energy associated with increasing cusp size.

Alternately, one might argue that the local behaviour in run-up observed in the bays is caused by increased infragravity energy in the bays caused by a free standing edge wave structure superimposed on the swash. However, *Bryan and Coco* [2007] use synthetic shuffled timeseries (with the same probability density functions of swash maxima and period as the data, but the swash cycles randomly ordered) with a superimposed infragravity signal to show the impact of an infragravity signal is to increase the optimum k and m (in that such signals are better predicted with a more global model) This is also evident in Case 7 (Figure2). An infragravity wave in the surfzone will affect the swash timeseries as a whole and therefore will not cause more local behaviour. Moreover, there was no evidence that the infragravity energy in *Ciriano et al*. [2005] (the same dataset as used here) was standing in the alongshore.

Although there were no substantial differences in the offshore wave climate between high and low tide on the 6th, there were changes to the inshore time series which might influence run-up behaviour. Firstly, the harmonic in the timeseries disappeared, so the mixture of high and low waves was not there at low tide (Figure 4). This was also evident in the spectrum, where the peak at the harmonic disappeared at low tide (Figure 5). This change was manifest as a change in the locality of the model (Figure 11A) at $d<T$, which is an indication that breaking influences the shape of waves, and the spectral width of the incident peak. Most importantly, the forecast at $d>T$ remained global both inside and offshore, regardless of tidal stage or wave conditions. There is no evidence of sequencing in the incoming wave field.

In the case of the forecasting results from September 4th, when the wave period is smaller and wave breaking more intense, the forecasting model does indeed have a significant drop in ability to forecast the run-up (the correlations dropping below ~0.1 which close to the significance level), which is accompanied by an increase in k and m, to the point where at $d>T$ the global model prevails. This decrease in forecasting ability between the inshore and run-up timeseries

was not evident on the day where cusps existed. This is most certainly partially due to the increased process noise in the timeseries caused by breaking on this higher energy day. The wave breaking, the flat topography, and higher energy and shorter period of the incoming waves combine to remove all nonlinearity (as evidenced by both the bispectral signature and the local behaviour) from the timeseries.

Although our findings show no evidence of interactions between swash causing infragravity signals on the flat beach case, our results are from a day when the incoming wave height was quite large, and there was a lot of wave breaking. It is certainly possible that longer-period incoming waves with less breaking could cause the very ordered interaction needed to cause the local behaviour and subharmonic-incident wave coupling, providing a mechanism for infragravity generation in the swash as suggested by, for example, Brocchini and Baldock [2008] and Baldock et al. [1997]. In our case, it was evident in the bays because the channelized down-rush so effectively enhanced the interaction to the extent where it could overcome the influence of noise on the statistical techniques.

Conclusions

The presence of beach cusps leads to alongshore variations in the nature of swash hydrodynamics. Past work has shown that this changes the energy levels at incident and infragravity frequencies, but has not provided conclusive insight into the causes of these differences. The non-linear forecasting results have shown that these energy level variations are accompanied by alongshore changes to the localness of the timeseries, which are most likely driven by interactions between subsequent swash events. The probability of interaction is controlled by the relationship between the incoming wave period and the run-up amplitude, and is driven largely by the control of beach slope on the latter. The interaction is complex because of the added influence of freely-propagating incident wave harmonics in the inner surf zone. Moreover, it is also likely that channelling of the downrush caused by the beach cusp geometry alone can increase the intensity of the swash interactions in the bay and contribute to local behaviour in the bay.

The observed local behaviour in the timeseries at beach cusp bays cannot be explained by the influence of alongshore patterning in surfzone infragravity waves such as caused by standing edge waves. However, the swash interactions in the timeseries can cause irregular, localised long-period oscillations in the timeseries, which bispectral analysis indicate are phase-locked to the incident waves. This provides a mechanism for the transfer of energy from incident waves to infragravity waves at least intermittently. The cuspate topography provides a regular alongshore scale to these temporally-irregular oscillations. Therefore run-up interactions in the bay provide a mechanism for the growth of infragravity waves in the swash in the presence of beach cusps, with alongshore wavenumbers governed by the cusp lengthscale. Our work clearly demonstrates that swash interactions can be a critical link between the surfzone and the evolving cusp morphology.

Acknowledgements

Planning and execution of the DozerDuck field experiment was led by B. T. Werner supported by an Office of Naval Research (ONR) Young Investigator Award (N00014-92-J-1446) and ONR, Coastal Dynamics. We wish to thank the many people that provided field assistance during the swash and surf zone experiments. Qingping Zou at University of Plymouth provided assistance with bispectral analysis. GC funded by the (New Zealand) Foundation for Research, Science and Technology. The clarity of the paper was improved immensely by comments from the associate editor and two anonymous reviewers.

References

Abarbanel, H. D. I. (1986), *Analysis of Observed Chaotic Data*, Institute for Nonlinear Science, 272pp, Springer, New York.

Baldock, T. E., P. Holmes, and D. P. Horn (1997), Low frequency swash motion induced by wave grouping, *Coastal Engineering 32,* 197–222.

Bowen, A. J. (1997), Patterns in the water: Patterns in the sand?, in *Coastal Dynamics '97*, edited by E. B. Thornton, pp. 1 – 10, Am. Soc. of Civ. Eng., Reston, Va.

Brocchini, M. and T. E. Baldock (2008), Recent advances in modeling swash zone dynamics: influence of surf-swash interaction on nearshore hydrodynamics and morphodynamics, *Reviews of Geophysics, 46*, doi: 8755-1209/08/2006RG000215.

Bryan, K. R. and G. Coco (2007), Detecting nonlinearity in run-up on a natural beach, *Nonlinear Processes in Geophysics*, *14*, 385–393.

Ciriano, Y., G. Coco, K. R. Bryan, and S. Elgar (2005), Field observations of swash zone infragravity motions and beach cusp evolution, *J. Geophys. Res*, *110*, C02018, doi: 10.1029/2004JC002485.

Coco, G., T. J. O'Hare, and D. A. Huntley (1999), Beach cusps: a comparison of data and theories for their formation, *J. Coastal Res*., *15*(3), 741–749.

Coco, G., T. K. Burnet, B. T. Werner, and S. Elgar (2003), Test of self-organization in beach cusp formation, *J. Geophys. Res*., *108*(C3), 3101, doi:10.1029/2002JC001496.

Cuomo, V., V. Lapenna, M. Macchiato, C. Serio, and L., Telesca (1998), Linear and nonlinear dynamics in electrical precursory time series: implications for earthquake prediction, *Tectonophysics, 287*, 279–298.

Elgar, S., and R. T. Guza (1985), Observations of bispectra of shoaling surface gravity waves, *J. Fluid. Mech. 161*, 425–448.

Elgar, S., R. T. Guza, B. Raubenheimer, T.H.C. Herbers, and E.L. Gallagher (1997), Spectral evolution of shoaling and breaking waves on a barred beach, *J. Geophys. Res., 102*(C7), 15797–15805.

Farmer, J.D., and J. J. Sidorowich (1987), Predicting chaotic time series, *Phys. Rev. Lett*. *59*, 845–848.

Gallagher, E.L., W. Boyd, S. Elgar, R.T.Guza, and B.Woodward (1996), Performance of a sonar altimeter in the nearshore, *Mar. Geol*., *133*, 241–248.

Hasselmann, K., W. Munk, and G. MacDonald (1963), Bispectra of ocean waves, in *Time Series Analysis*, edited by M. Rosenblatt, pp. 125– 139, John Wiley.

Herbers, T.H.C., N.R. Russnogle, and S. Elgar, 2000 Spectral energy balance of breaking waves within the surf zone, *J. Phys. Ocean.*, *30*(11), 2723–2737.

Holland, K.T., and R.A. Holman (1996), Field observations of beach cusps and swash motions, *Mar. Geol*., *134*, 77–93.

Holland, K. T., C. L. Vincent, and R. A. Holman (1999), Statistical characterisation of nearshore morphodynamic behaviour, in *Coastal Sediments '99*, edited by N. C. Kraus, pp. 2176–2189, Am. Soc. of Civ. Eng., New York.

Huntley, D.A., R.T. Guza, and A.J. Bowen (1977), A universal form for shoreline run-up spectra?, *J. Geophys. Res*., *82*(18), 2577–2581.

Jaffe, B.E., and D.M. Rubin (1996), Using nonlinear forecasting to learn the magnitude and phasing of time-varying sediment suspension in the surf zone, *J. Geophys. Res*., *101*(C6), 14283–14296.

Mase, H. (1988), Spectral characteristics of random wave run-up, *Coast. Eng.*,*12*, 175–189.

Masselink, G., B.J. Hegge, and C.B. Pattiaratchi (1997), Beach cusp morphodynamics, *Earth Surface Processes and Landforms*, *22*, 1139–1155.

Masselink, G., and C.B. Pattiaratchi (1998), Morphological evolution of beach cusp morphology and associated swash circulation patterns, *Mar. Geol*., *146*, 93-113.

Pape, L., and B.G. Ruessink (2008), Multivariate analysis of nonlinearity in sandbar behaviour, *Nonlinear Processes in Geophysics*, *15*, 145–158.

Raubenheimer, B., and R. T. Guza (1996), Observations and predictions of run-up, *J. Geophys. Res*., *101*(C11), 25,575.

Rubin, D. M. (1992), Use of forecasting signatures to help distinguish periodicity, randomness, and chaos in ripples and other spatial patterns, *Chaos, 2*, 525–535.

Rubin, D. M. (1995), Forecasting techniques, underlying physics and applications, in *Nonlinear Dynamics and Fractals: New Numerical Techniques for Sedimentary Data*, edited by G. V. Middleton, R. E. Plotnick and D. M. Rubin, SEPM Short Course No. 36. , 174pp, Society for Sedimentary Geology.

Ruggiero. P., R. A. Holman, and R. A. Beach (2004), Wave run-up on a high-energy dissipative beach, *J. Geophys. Res*., *109*, C06025, doi:10.1029/2003JC002160.

Shen, M. C. and R. E. Meyer (1963), Climb of a bore on a beach: 3. Run-up. *J. Fluid Mech., 16(8),* 113–135.

Small, M., and C. K. Tse (2002), Applying the method of surrogate data to cyclic timeseries, *Physica D 16*4, 18–201.

Sugihara, G. (1994), Nonlinear Forecasting for the Classification of Natural Time Series, *Phil. Trans. R. Soc. Lond. A, 348*, 477–495.

Sugihara, G., and M. R. May (1990), Nonlinear forecasting as a way of distinguishing chaos from measurement error in time series, *Nature, 344*, 734–741.

Figure Captions:

Figure 1: Cases 1–5 synthetic timeseries. Column 1: Narrow-banded timeseries, reconstructed from spectrum using randomised phases. Column 2: Broad-banded timeseries, reconstructed from spectrum using randomised phases. Column 3: Time series of Stokes waves. Column 4: Timeseries of inverted Stokes waves, where every second wave is larger. Column 5: Mixture of 50% of the case shown in column 4, and 50% of case shown in column 3, inverted, with ordering of the mixture determined randomly. In all cases, the spectral peak frequency is 0.1Hz, and timeseries have been demeaned and normalised to unit variance. Panels A: Example timeseries. Panels B: Bicoherence, with 84 degrees of freedom. Bicoherence levels below the 95% confidence limits are blanked. Panels C: Spectral densities, calculated using a Tukey-Hamming window resulting in 50 degrees of freedom. Panels D: The greyscale shows correlation between actual and predicted timeseries as a function of number of nearest neighbours, k, and plaquette length, m, at $d=4*\Delta t$ steps into the future where, $\Delta t=5,4,6,8,7$ points, equating to $d=10, 8, 12, 16, 14$ seconds into the future for each column respectively. The plaquette size that was used is given in points on the left axis, and in seconds on the right axis. Note the different grayscales. The optimal m and k, calculated using a polynomial fit, are marked with a circle.

Figure 2: Case 6–10 synthetic timeseries. Column 1: Generated by randomly modulating the starting velocity and period to simulate groupiness in the incoming waves. Column 2: No modulation to the starting velocity and period but a superimposed infragravity wave. Column 3: Weak interaction between swash cycles with the degree of randomness modulated through out the series to simulate local behaviour. Column 4: The same as the case shown in column 3, except with a stronger modulation. Column 5: Same as the case shown in column 3, except with a greater variation of the degree of randomness. In all cases, the spectral peak frequency is 0.06Hz and beach slope is 0.01 (chosen to ensure swash cycles interact), and timeseries have been demeaned and normalised to unit variance. Panels A: Example timeseries. Panels B: Bicoherence,

with 84 degrees of freedom. Bicoherence levels below the 95% confidence limits are blanked. Panels C: Spectral densities, calculated using a Tukey-Hamming window resulting in 50 degrees of freedom. Panels D: The greyscale shows correlation between actual and predicted timeseries as a function of number of nearest neighbours, k, and plaquette length, m, at $d=4*\Delta t$ steps into the future where, $\Delta t=11,10,11,10,11$ equating to $d=22,20,22,20,22$ seconds into the future for each column respectively. The plaquette size that was used is given in points on the left axis, and in seconds on the right axis. Note the different grayscales. The optimal m and k, calculated using a polynomial fit, are marked with a circle.

Figure 3:

The enhancement of the local model prediction ability relative to the global, as a function of the percentage mixture of two series: Case 4 and Case 3 (inverted) in Figure 1. A measure of enhancement is the correlation between prediction and original timeseries at optimum k and m divided by the correlation at maximum k and optimum m.

Figure 4:

Example time series for: Right panels: sea surface elevation at location 398m offshore from the origin of the surveying grid (the single bar is at 240m offshore and the shoreline is at approximately 120m). Middle panels: sea surface elevation inshore of the bar at 145m offshore. Left panels: Swash timeseries at horn (continuous line) and bay (dashed line) positions. Top panel ('flat'): Time series collected on the 4th of September when the beachface was flat (timeseries are separated by the same distance as the timeseries shown from the day with cusped topography). Middle panel ('High tide'): Time series collected at high tide on the 6th of September when cusps were present. Bottom panels ('Low tide'): Time series collected at low tide on the 6th of September when cusps were present. Horn and bay time series are synchronous with each other and offshore and inshore time series are synchronous with each other.

Figure 5: Spectra of the timeseries shown in Figure 4, calculated using a Tukey-Hamming window giving 54 degrees of freedom. See caption of Figure 4 for details.

Figure 6: Grey scale represents correlations between forecast and swash data taken at a horn (alongshore location: 860m, position 5) and bay (alongshore location: 870m, position 7) as a function of embedding dimension m and number of nearest neighbours k at forecasting distance $d=\Delta t$, where Δt is 7 and 10 points respectively. The optimal m and k calculated using a polynomial fit are marked with a circle. The significance level is approximately 0.05.

Figure 7: Panel A: beach face survey on September 6th. Contour heights are at 0.25m intervals. The location of the shoreline at high and low tide (with one swash elevation standard deviation added) are plotted with lines and crosses. The alongshore location where swash timeseries were extracted are plotted with dashed lines, and the location of the cross-shore array of pressure sensors is marked with a thick black line. Panel B: The greyscale indicates the correlation values at different distances into the future where d=1,2,3 …means $d = \Delta t, 2\Delta t, 3\Delta t...$ The top scale and the line correspond to the optimum k at d = 1. Panel C: Same as in Panel B, only for low tide on September 6th.

Figure 8: Panel A: Correlation between forecast and data at the optimal m and k as a function of prediction distance into the future. Panel B: The optimum k as a function of d. Panel C: The optimum m as a function of d. In all cases, the dashed lines are for low tide and solid lines for high tide Lines with circles are for horns and lines with no circles are for the bays. Results have been averaged for series at the horns and bays and the error bars indicate the standard error.

Figure 9: Panel A: Correlation as a function of beach slope. Panel B: Optimum k as a function of beach slope. Panel C: Optimum m as a function of beach slope. All cases are for a prediction distance $d = 1$.

Figure 10: Left Panel: Survey beachface morphology on September 4th. Contour heights are at 0.25m intervals. The location of the shoreline at high and low tide (with one swash elevation standard deviation added) are plotted with lines and crosses. The alongshore location where swash timeseries were extracted are plotted with dashed lines, and the location of the cross-shore array of pressure sensors is marked with a thick black line. Right Panel: Grey scale corresponds to the correlation (significance level based on the analysis of other series is assumed to be ~ 0.05,

see text) as a function of distance (in points) and alongshore location. The line and top scale show the optimum k at d=1.

Figure 11: Panels A and B: Optimum number of nearest neighbours k plotted against forecasting distance for the forecasting results applied to the sea surface elevation timeseries: Solid lines: inshore at 145m offshore and dashed lines 884m offshore. The dashed vertical lines indicate the peak spectral period (the separation between $d<T$ and $d>T$). Panel A: High tide of September 6th, '-' low tide September 6th, 'o'. Panel B: high tide September 4th, '-' low tide September 4th, 'o'. Panel C: The cross-shore distribution of correlation at the optimum k and m at $d=4\Delta t$ (which is greater than T). Solid lines are for high tide, and dashed lines are for low tide. The lines with stars are for September 4th (with the higher wave energy) and the lines without stars are for September 6th. Note the innermost points at low tide should be disregarded as examination of the timeseries indicates that the sensor was exposed during wave troughs. Panel D: surveyed depth profile.

Figure 12:

Panel A: Beach topography on September 6th. Panel B: Alongshore variation of bicoherence (solid line, scale at top), with 95% significance level marked as a dashed line and biphase (line with circles, scale at the bottom) of the coherent peak at (f/2,f/2). Bicoherence and phase were run with a 1024-point Fourier transform and the results merged over 12 frequency bins. Panel C: Bicoherence averaged for all timeseries collected at or near a horn, signals below the 95% significance level have been blanked (also blanked in remaining panels). Panel D: Biphase averaged for all timeseries collected at or near a horn. Panel E: Bicoherence averaged for all timeseries at or near a bay. Panel F: Biphase for all timeseries at or near a bay.

Table 1: Summary of the results of forecasting and bispectral analysis for all cases. 'Synthetic' refers to the results from the synthetic models, Cases 1–5 are presented in Figure 1 and Cases 6–10 are presented in Figure 2. 'Horn swash high tide', 'Bay swash high tide', 'Horn swash low tide', 'Bay swash low tide' represent the averaged results for all timeseries collected near the horn and bay positions at high tide and low tide. 'Flat low tide' shows the averaged results for timeseries collected on the 4th of September when the beachface was flat. 'Inshore' and 'offshore' represent the results for sea surface elevation at location at 145m and 398m offshore from the origin of the surveying grid (the single bar is at 240m offshore and the shoreline is at approximately 120m) at high tide only. Plaquette size (m) is given in points and in seconds ($m\Delta t$). Number of nearest neighbours k is given in points and also as a percentage of the whole series, where k_{opt} and k_{global} are for the optimal and global forecasts respectively. The enhancement of the local model is summarised as the correlation at optimum k ($\rho(k_{global})$) divided by the correlation at global k ($\rho(k_{global})$). The forecasting results are for a forecasting distance that is greater than one swash cycle. (The significance level for the bicoherence is 0.26.)

Case	m_{opt} *(pts,s)*	k_{opt} *(pts,%)*	$\rho(k_{opt},m_{opt})$	$\rho(k_{opt})/\rho(k_{global})$	*Bispectral coherence at f/2, f/2*
Synthetic 1	12,30	14000, 100	1.00	100.00	0.13
Synthetic 2	11,22	14000, 100	0.03	100.00	0.17
Synthetic 3	10,30	14000, 100	1.00	100.00	0.13
Synthetic 4	3,12	3853,28	1.00	100.04	0.48
Synthetic 5	9,31.5	158,1	0.97	111.54	0.46
Synthetic 6	12,66	14000, 100	0.31	100.00	0.57
Synthetic 7	12,66	126,<1	1.00	100.02	0.09
Synthetic 8	5,27.5	970,4	0.97	112.42	0.76
Synthetic 9	5,25	67,<1	0.96	104.22	0.79
Synthetic 10	5,27.5	709	0.76	125.19	0.67
Horn swash high tide	7,25	2549,18	0.52	103.41	0.18
Bay swash high tide	4,20	1319,9	0.29	123.7	0.38
Horn swash low tide	8,32	5822,42	0.31	99.43*	0.22
Bay swash low tide(6th)	7,30.5	2838,20	0.28	101.91	0.21
Flat swash low tide (4th)	7,27	12300,88	0.13	99.82*	0.22
Inshore, high tide (6th)	10,20	10405,74	0.37	101.20	0.16
Offshore, high tide (6th)	11,28	14000, 100	0.69	100.00	0.18
Inshore, high tide (4th)	12,24	14000, 100	0.23	100.00	0.29
Offshore, high tide (4th)	11,22	14000, 100	0.56	100.00	0.16

*This is essentially 100%, fraction is calculated after averaging, and we are averaging across timeseries that vary between slightly local and slightly global.

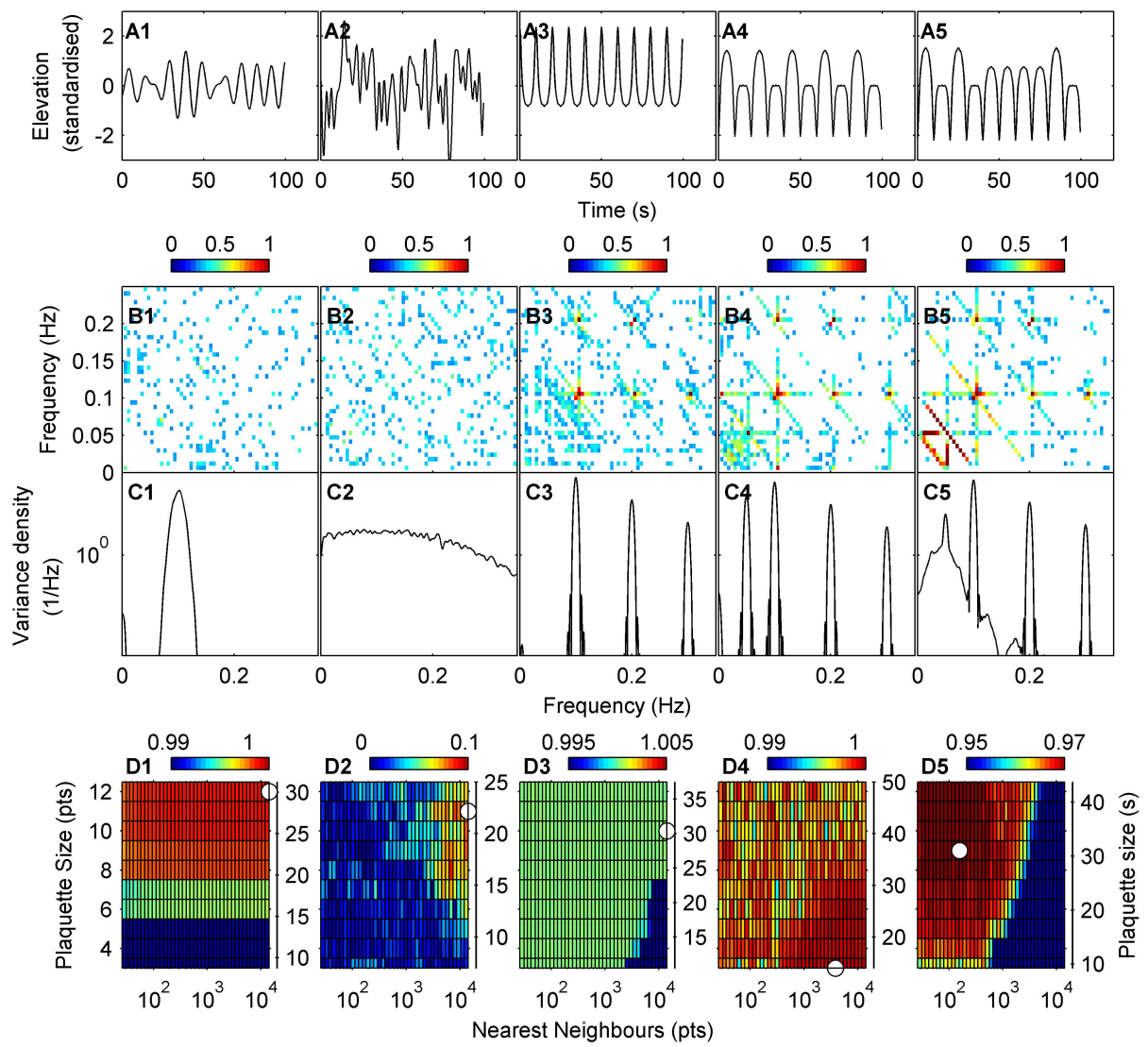
A1
A2
A3
A4
A5
Elevation (standardised)
Time (s)
B1
B2
B3
B4
B5
Frequency (Hz)
C1
C2
C3
C4
C5
Variance density (1/Hz)
Frequency (Hz)
D1
D2
D3
D4
D5
Plaquette Size (pts)
Plaquette size (s)
Nearest Neighbours (pts)

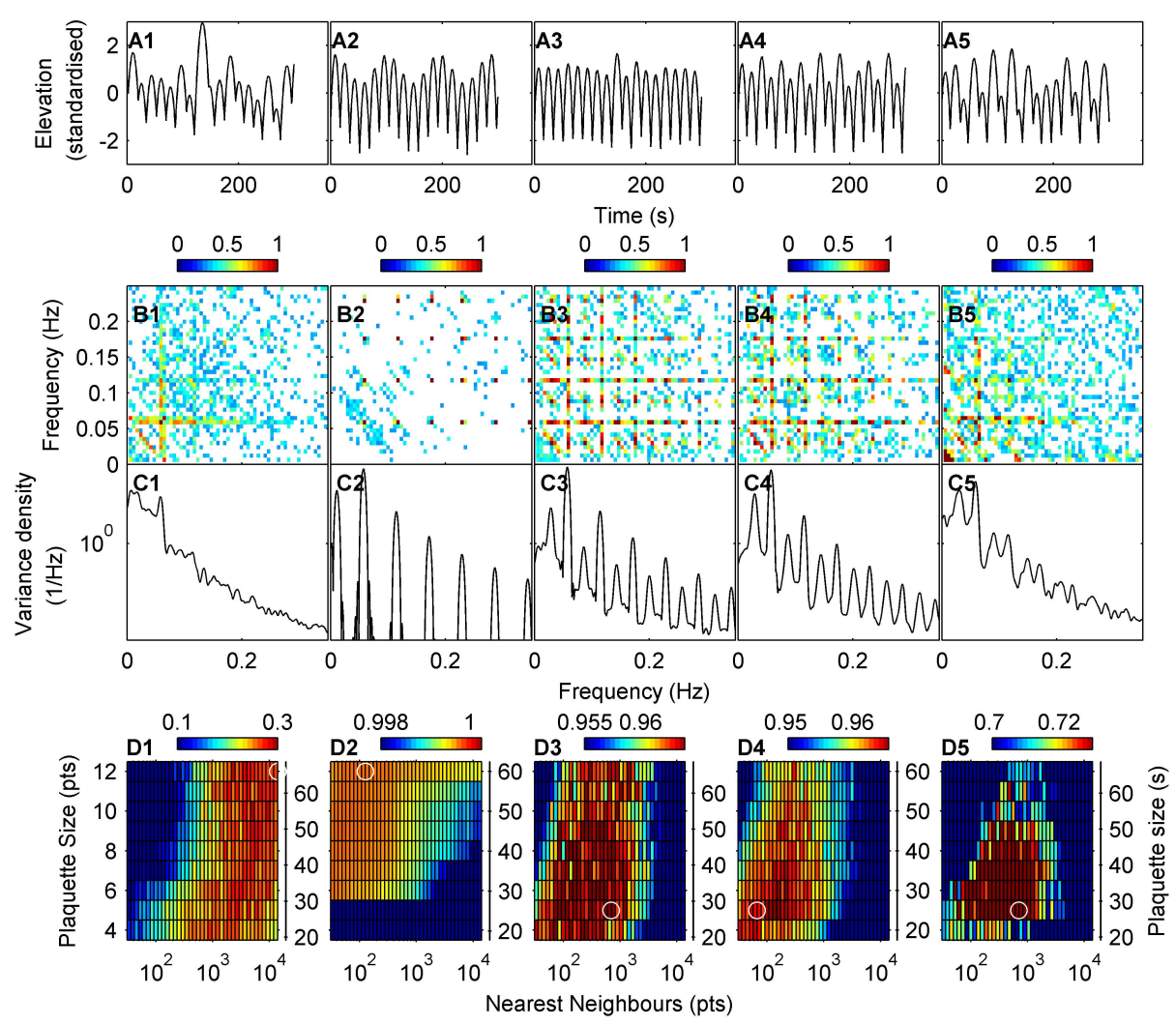
A1
A2
A3
A4
A5
Elevation (standardised)
Time (s)
B1
B2
B3
B4
B5
Frequency (Hz)
C1
C2
C3
C4
C5
Variance density (1/Hz)
Frequency (Hz)
D1
D2
D3
D4
D5
Plaquette Size (pts)
Plaquette size (s)
Nearest Neighbours (pts)

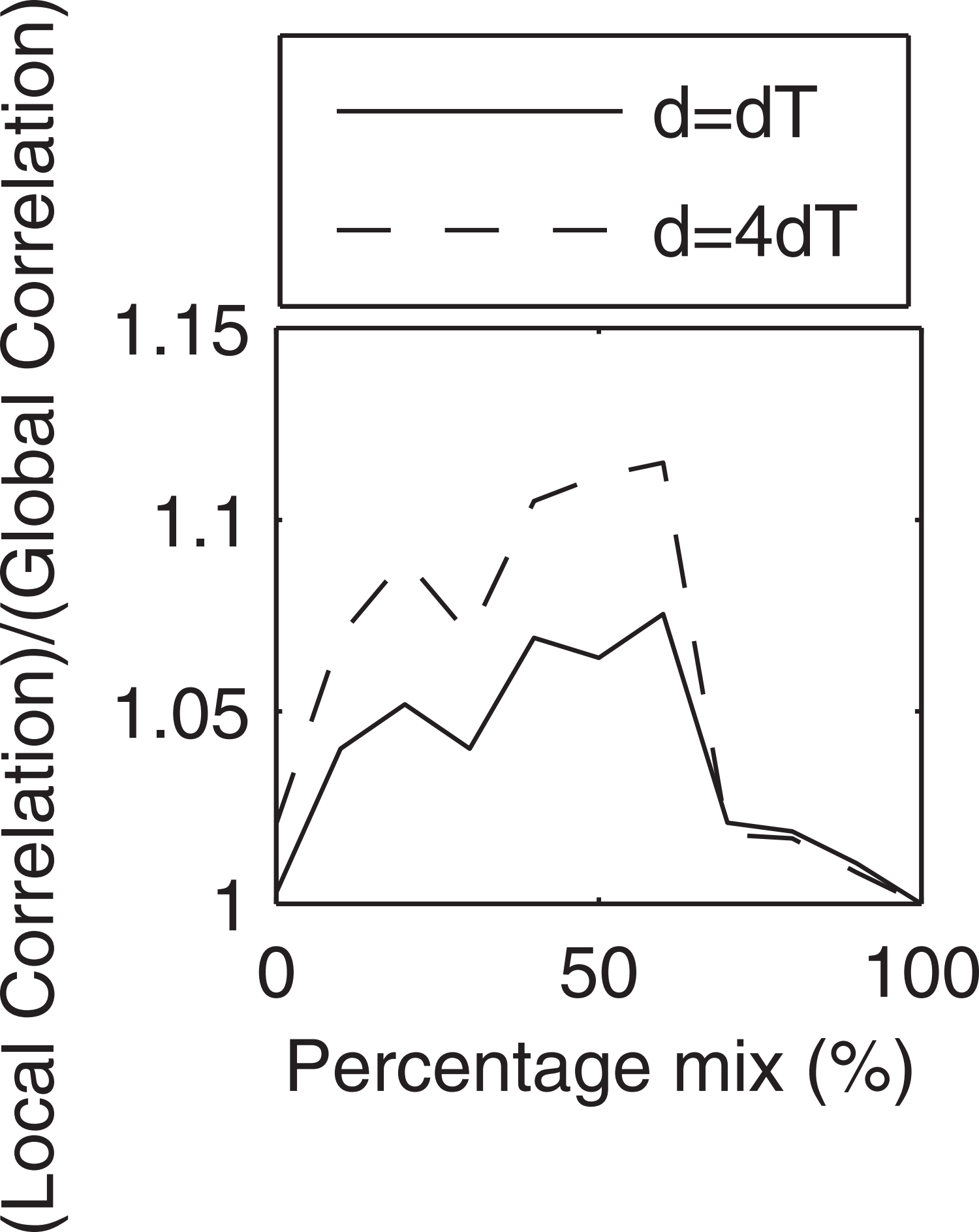
d=dT
d=4dT
1.15
1.1
1.05
1
0
50
100
Percentage mix (%)
(Local Correlation)/(Global Correlation)

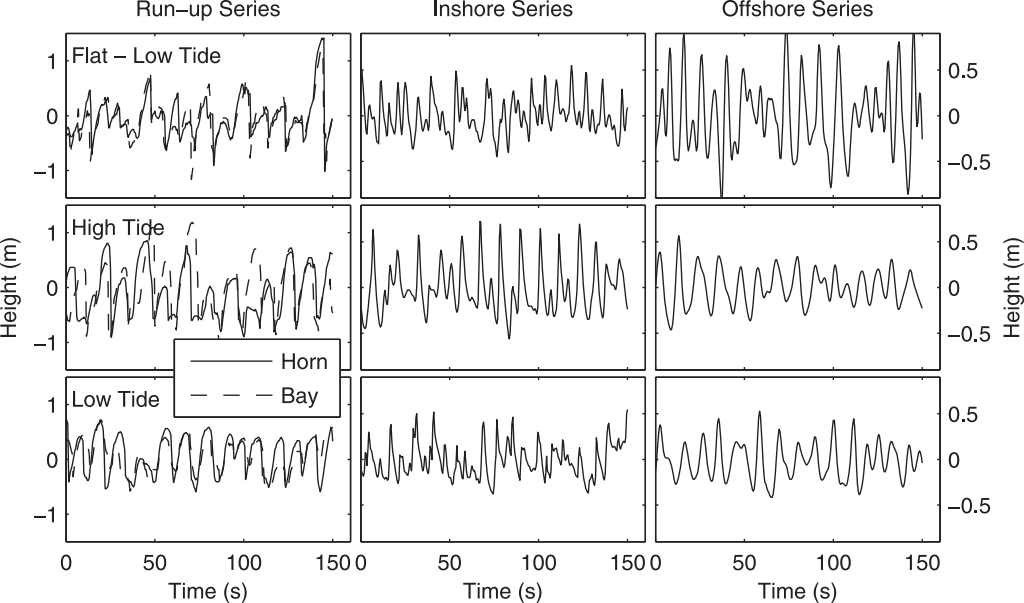
Run–up Series
Inshore Series
Offshore Series
Flat – Low Tide
High Tide
Low Tide
Horn
Bay
Height (m)
Height (m)
Time (s)
Time (s)
Time (s)
1
0
−1
0.5
0
−0.5
0
50
100
150

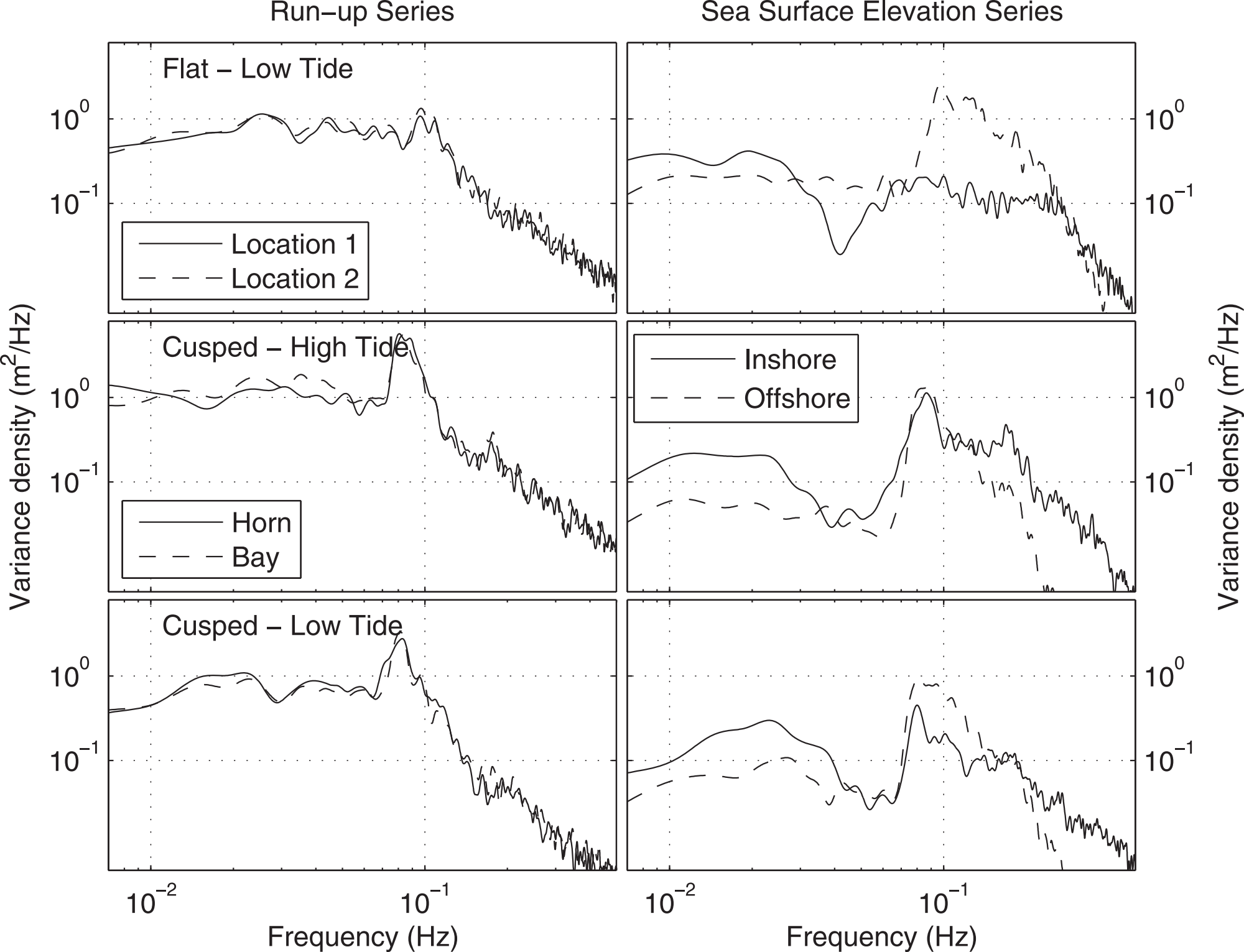
Run–up Series
Sea Surface Elevation Series
Flat – Low Tide
Location 1
Location 2
Cusped – High Tide
Horn
Bay
Inshore
Offshore
Cusped – Low Tide
Variance density (m²/Hz)
Frequency (Hz)

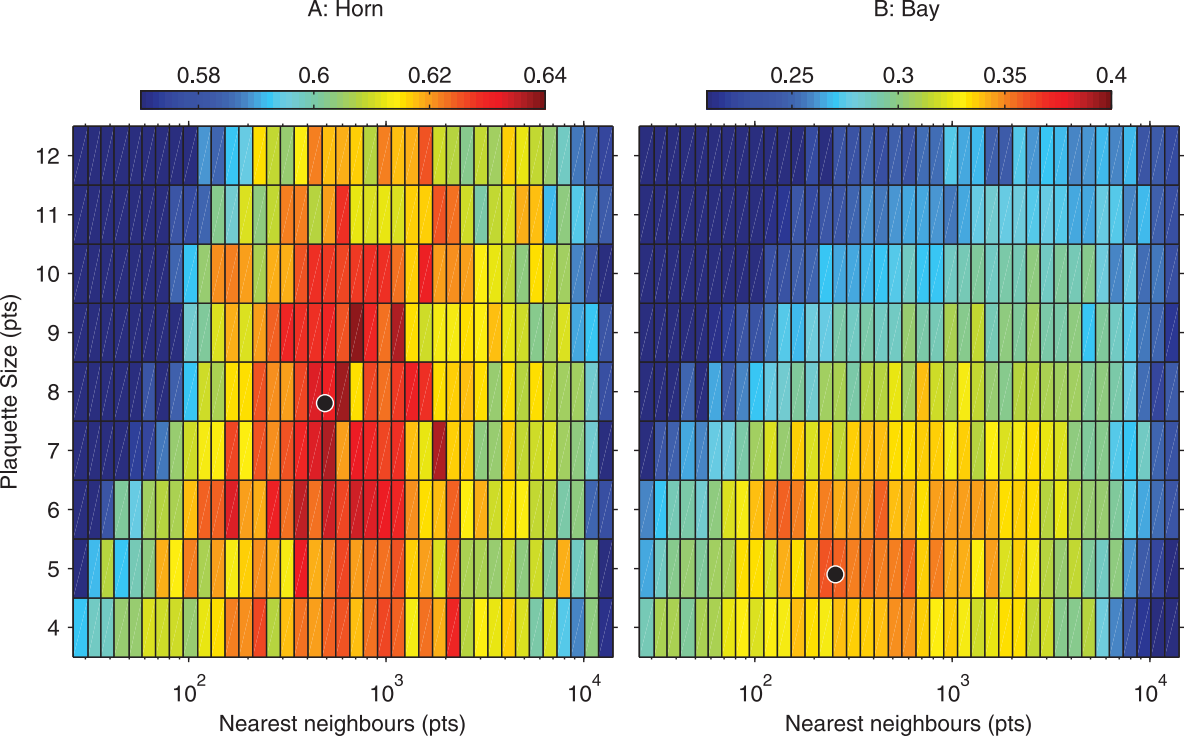
A: Horn
B: Bay
0.58
0.6
0.62
0.64
0.25
0.3
0.35
0.4
Plaquette Size (pts)
12
11
10
9
8
7
6
5
4
10^2
10^3
10^4
Nearest neighbours (pts)
Nearest neighbours (pts)

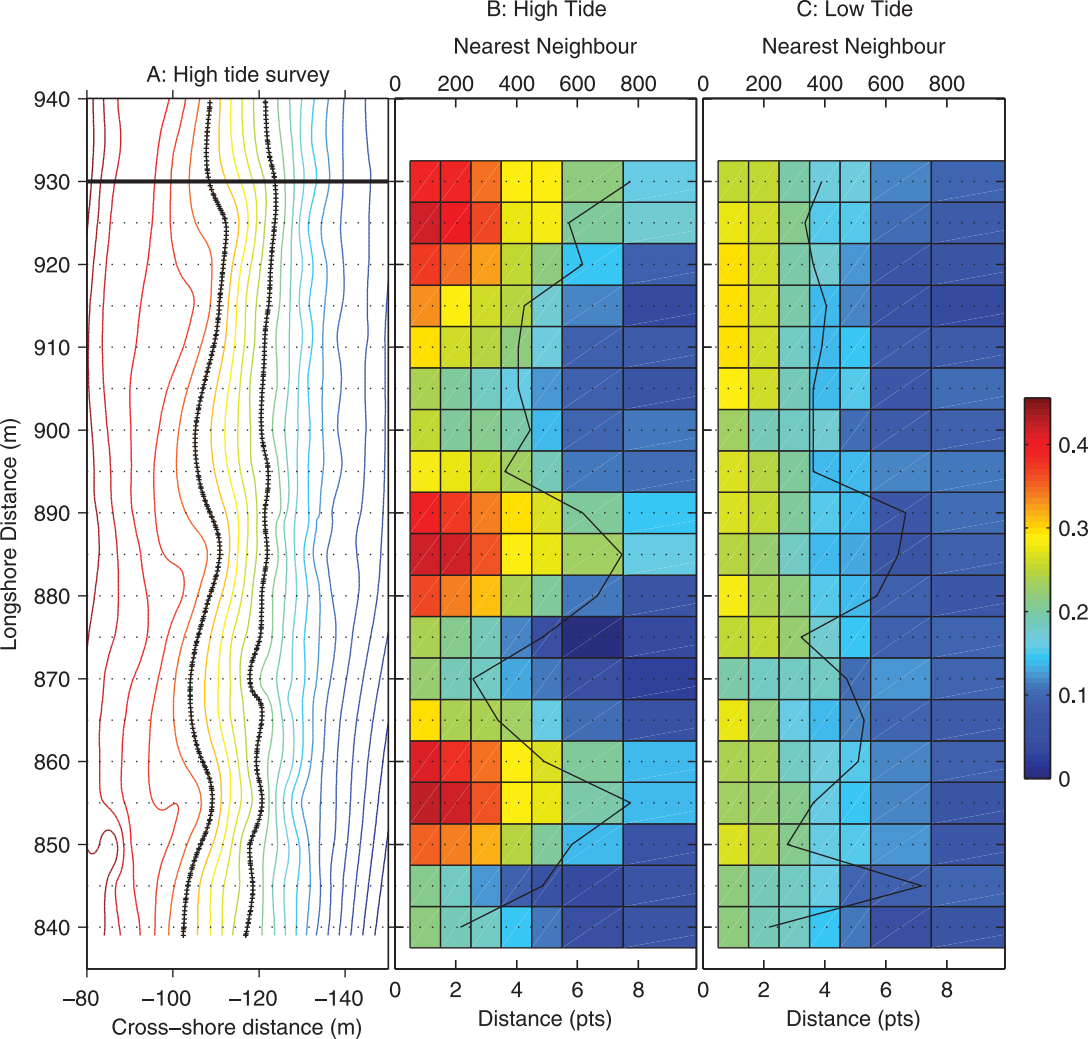
A: High tide survey
B: High Tide
Nearest Neighbour
C: Low Tide
Nearest Neighbour
Longshore Distance (m)
940
930
920
910
900
890
880
870
860
850
840
0
200
400
600
800
−80
−100
−120
−140
Cross−shore distance (m)
0
2
4
6
8
Distance (pts)
0.4
0.3
0.2
0.1
0

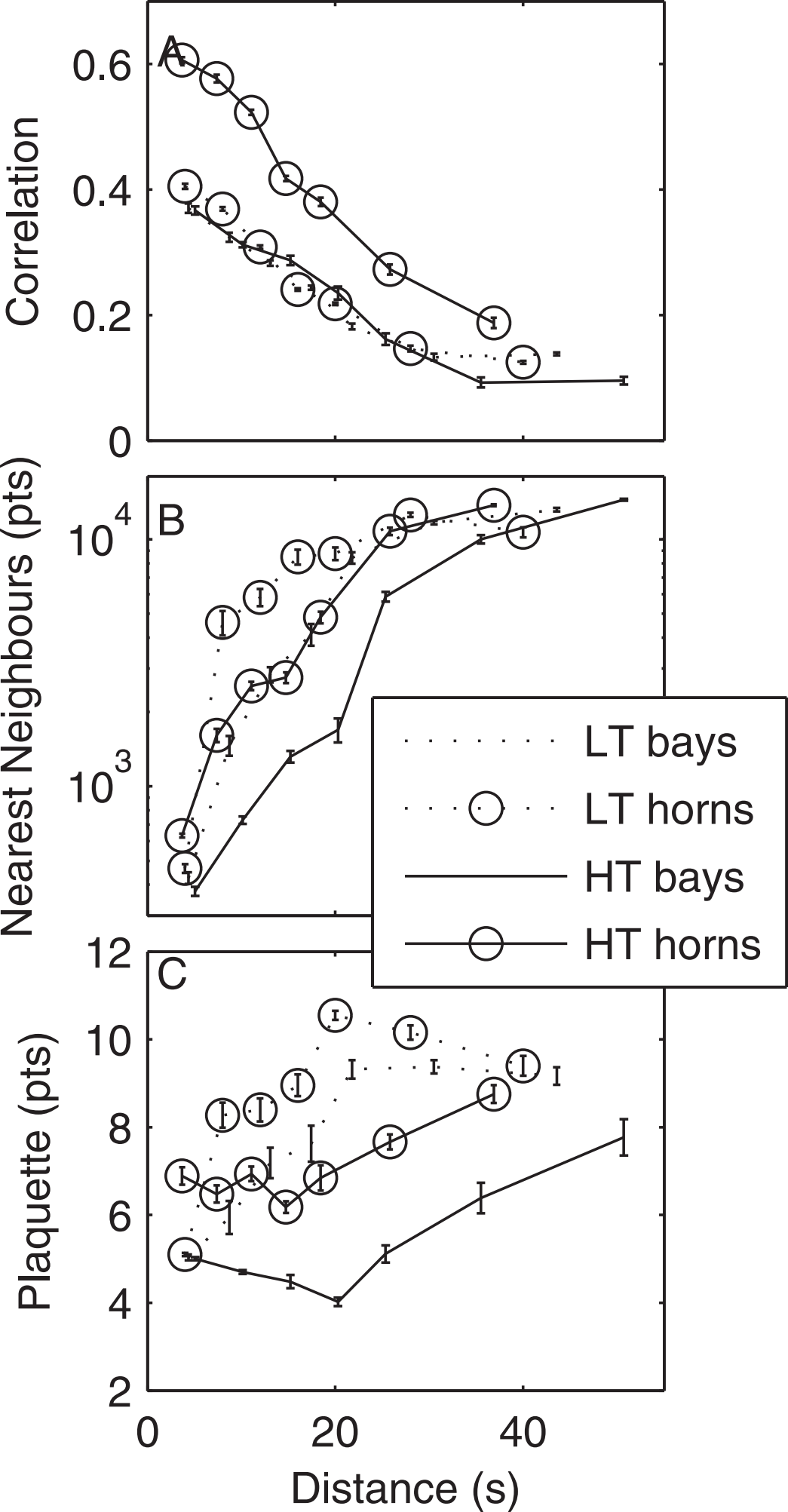
A
B
C
Correlation
Nearest Neighbours (pts)
Plaquette (pts)
Distance (s)
0.6
0.4
0.2
0
10^4
10^3
12
10
8
6
4
2
0
20
40
LT bays
LT horns
HT bays
HT horns

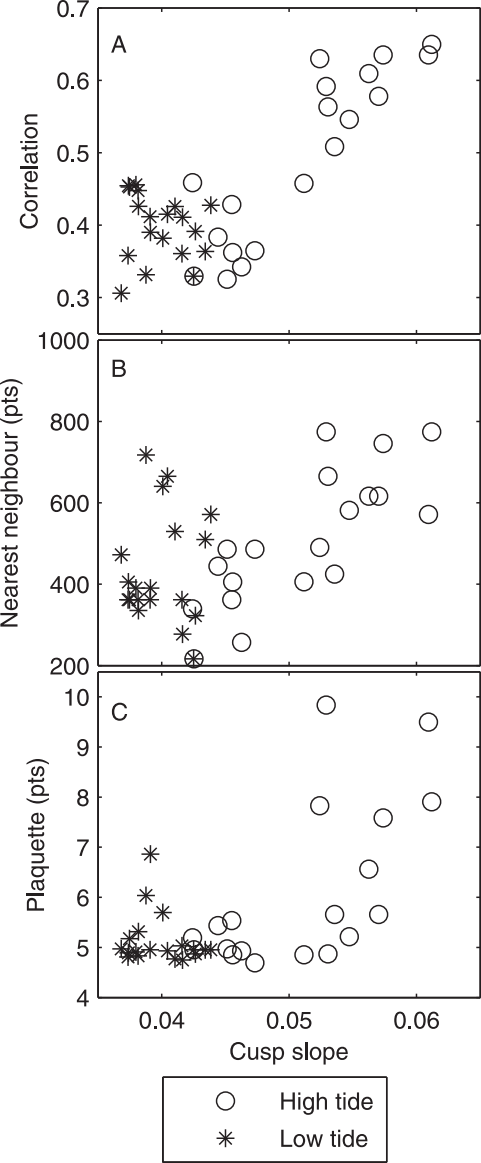
A
B
C
Correlation
Nearest neighbour (pts)
Plaquette (pts)
Cusp slope
0.7
0.6
0.5
0.4
0.3
1000
800
600
400
200
10
9
8
7
6
5
4
0.04
0.05
0.06
High tide
Low tide

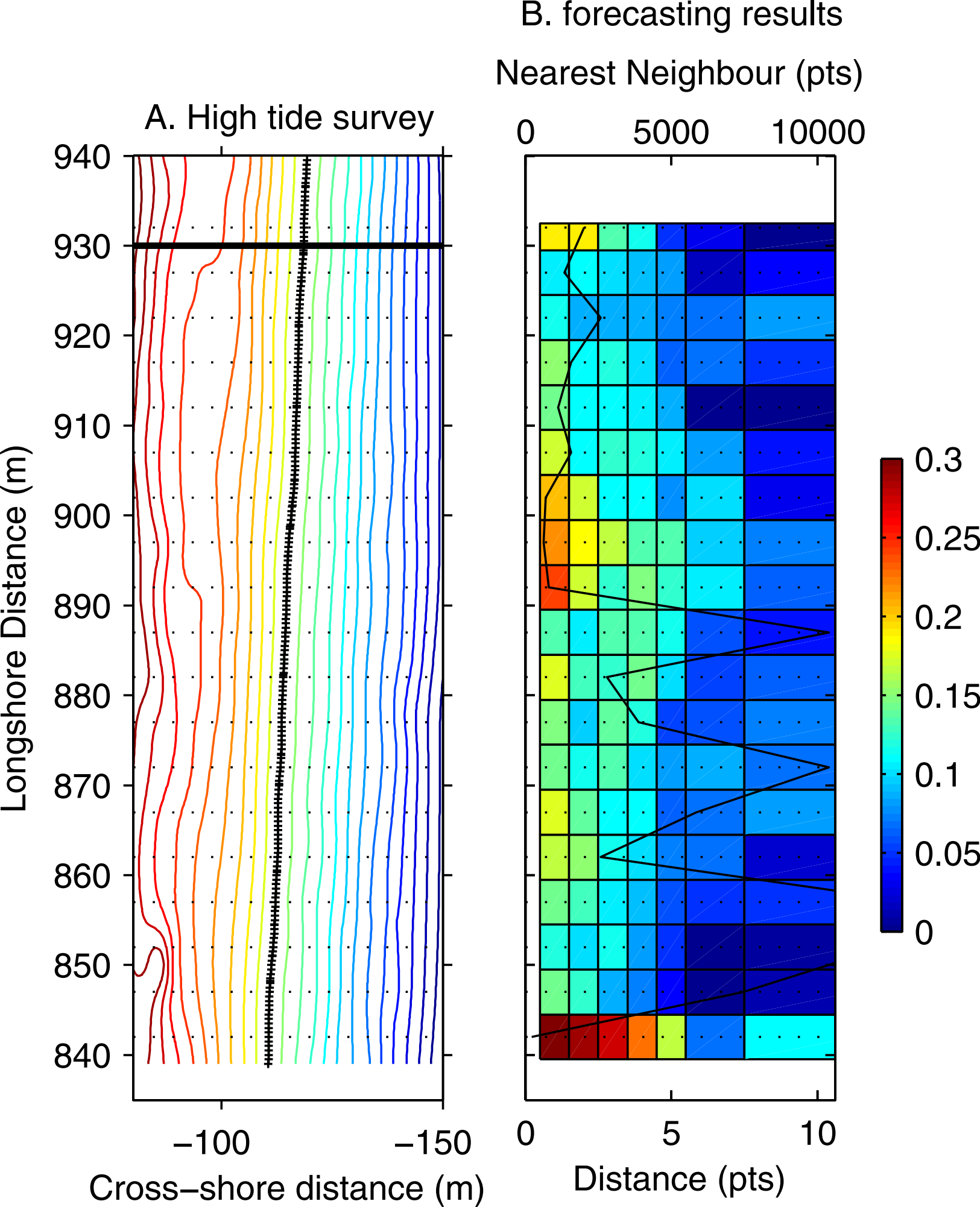
A. High tide survey
B. forecasting results
Nearest Neighbour (pts)
0
5000
10000
940
930
920
910
900
890
880
870
860
850
840
Longshore Distance (m)
−100
−150
Cross−shore distance (m)
0
5
10
Distance (pts)
0.3
0.25
0.2
0.15
0.1
0.05
0

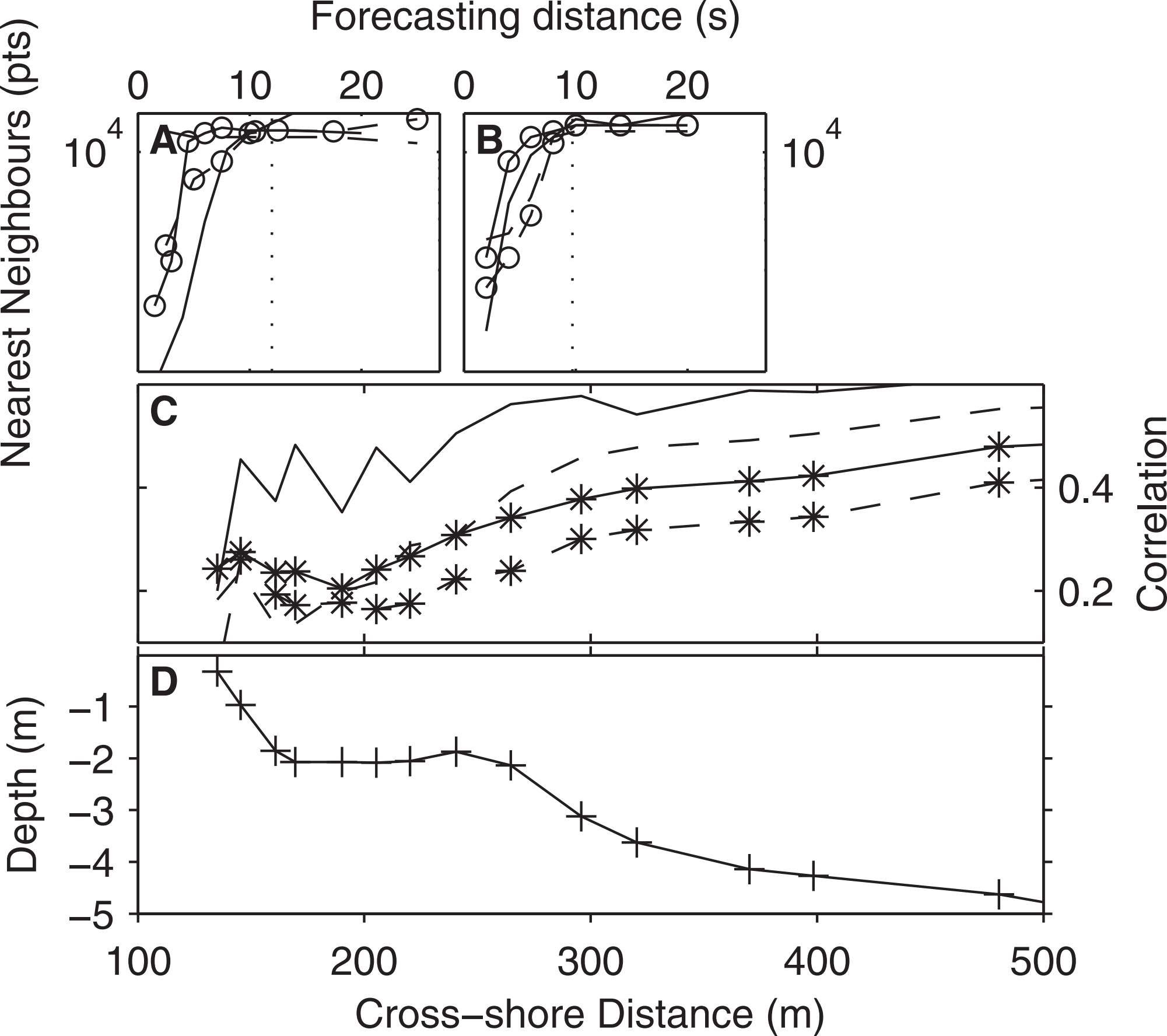
Forecasting distance (s)
0
10
20
0
10
20
Nearest Neighbours (pts)
10^4
A
B
10^4
C
0.4
0.2
Correlation
D
−1
−2
−3
−4
−5
Depth (m)
100
200
300
400
500
Cross−shore Distance (m)

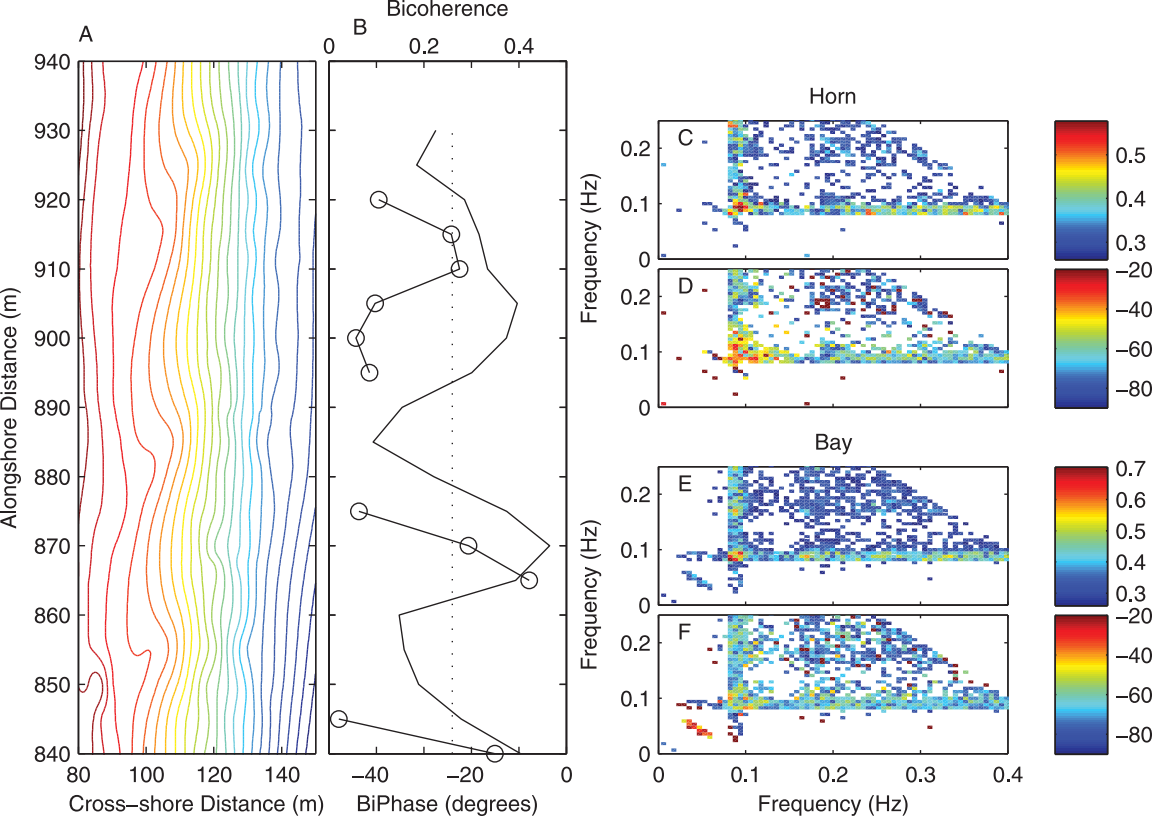
A
B
Bicoherence
0
0.2
0.4
940
930
920
910
900
890
880
870
860
850
840
Alongshore Distance (m)
80
100
120
140
Cross−shore Distance (m)
−40
−20
0
BiPhase (degrees)
Horn
C
D
Bay
E
F
Frequency (Hz)
0.2
0.1
0
0.3
0.4
0.5
0.6
0.7
−20
−40
−60
−80